A 3D face interpolated discretisation method for simulating anisotropic diffusive processes on meshes coming from wood morphology

El-Houssaine Quenjel, Patrick Perré, Ian Turner

A 3D face interpolated discretisation method for simulating anisotropic diffusive processes on meshes coming from wood morphology

El-Houssaine Quenjel[1], Patrick Perré[1] and Ian Turner[2]

[1]Chair of Biotechnology, LGPM, CentraleSupélec, Centre Européen de Biotechnologie et de Bioéconomie (CEBB), 3 Rue des Rouges Terres, 51110 Pomacle, France. el-houssaine.quenjel@centralesupelec.fr, patrick.perre@centralesupelec.fr

[2]School of Mathematical Sciences, Queensland University of Technology (QUT), Brisbane, Australia. i.turner@qut.edu.au

August 7, 2023

Abstract

In this paper, a new 3D numerical discretisation method for solving the anisotropic, steady-state diffusion problem is developed and analysed. The scheme is constructed on hexahedral meshes using the geometrical properties of the cells. Indeed, each cell provides a local basis formed using the centres of its lateral faces. The discrete cell gradient approximation is then obtained by using three discrete directional derivatives resolved in terms of this basis, and by invoking the consistent relationships between opposite faces of the same cell. The face degrees of freedom are interpolated to reduce the complexity of the numerical scheme, resulting in the main unknowns being entirely nodal based. The scheme is unconditionally coercive and admits a unique solution. Various numerical experiments are performed to highlight the accuracy and the robustness of the method with respect to the mesh and anisotropy. An important outcome is that second order convergence is observed for all problems considered, even for highly deformed meshes. After this validation process, the method is applied to the prediction of the effective thermal conductivity of wood from its real 3D morphology. The property

is estimated in the radial tangential and longitudinal directions. The solver is robust, efficient and yields to similar results compared to recent contributions.

Keywords: Diffusive equations, 3D discrete gradient, anisotropy, second order accuracy, wood morphology, thermal conductivity.

1 Introduction

Partial differential equations (PDEs) are present in an uncountable number of applications in science and engineering. As a consequence, there is an increasing demand for solving PDEs numerically. In particular, linear and nonlinear diffusion terms are crucial components of many physical systems and are used to model, for example, complex flows in porous media, and heat and mass transfer in highly heterogeneous materials such as wood and plant stems [27]. The discretisation of various types of diffusion problems (linear, nonlinear, transient or steady-state) on generic 3D meshes is a challenging topic because the reconstruction of the gradient from a finite set of points must be subject to consistency and stability rules. In this work we propose an original idea to devise a whole gradient across a hexahedral mesh that takes into account the shape and geometric properties of each cell. For this purpose, we will focus on a very standard linear, anisotropic Poisson equation arising in many applications.

Let Ω be an open bounded connected domain of $\mathbb{R}^3$. Let us consider the 3D elliptic model

$$\begin{cases} -\operatorname{div}(\Lambda \nabla u) = f, & \text{in } \Omega, \\ u = g, & \text{on } \partial\Omega, \end{cases} \tag{1}$$

where Λ is a symmetric positive-definite tensor defined from Ω to $L^\infty(\Omega)^{3\times 3}$ that fulfils the ellipticity condition

$$\lambda_0 \|\zeta\|^2 \leq \Lambda\zeta \cdot \zeta \leq \lambda_1 \|\zeta\|^2, \quad \forall \zeta \in \mathbb{R}^3,$$

and λ_0 and λ_1 are some positive constants. The source term is a function of $L^2(\Omega)$ and $g \in H^{1/2}(\partial\Omega)$. Under these assumptions, it is well-known that the model problem admits a unique weak solution $u \in H^1(\Omega)$ whose trace is g and solves the variational formulation

$$\int_\Omega \Lambda \nabla u \cdot \nabla \varphi \, \mathrm{d}x = \int_\Omega f\varphi \, \mathrm{d}x, \quad \forall \varphi \in H_0^1(\Omega). \tag{2}$$

During the last two decades, it has been established that a good and proper approximation of the gradient can lead to an efficient and accurate resolution of the problem (2). Depending on the data, namely Λ, f, g, Ω and the mesh, many numerical methods were developed to conceive approximate directional derivatives as in the finite difference approach. Their accuracy and robustness are observed through the FVCA benchmarks [16, 18]. Many of them share several common

points in terms of analysis, which renders them eligible to enter the theoretical framework called the gradient discretisation method [12]. This paradigm includes shape function based classical methods such as the $\mathbb{P}_1$-finite elements [7]. It also contains modern methods and we mention among them the Hybrid Mimetic Mixed approaches [10, 13, 15], Multi-Point Flux Approximations [1–3], Diamond schemes [9, 28], and Discrete Duality Finite Volume methods [4, 5, 8, 11, 19]. In addition to the primary degrees of freedom (DOFs), many of the aforementioned methods require auxiliary unknowns in the reconstruction of the gradient as the mesh becomes distorted.

In this work, we first propose and validate a new 3D numerical method for the resolution of (2). The motivation for this scheme results from the need to use distorted hexahedral meshes with larger sets of DOFs, without introducing auxiliary unknowns, as well as tackling the challenges of higher anisotropy ratios while still ensuring a straightforward implementation strategy. For instance, such constraints are naturally imposed during the prediction of macroscopic properties from real morphologies using computational homogenisation [6, 23, 24, 26, 30], or to track liquid imbibition in complex media such as natural wood [25].

The contribution of the paper is twofold. The first asset lies in the scheme construction. More importantly, the main idea of our work is to define the numerical scheme using only the geometrical information of the mesh cells. Indeed, following the spirit of the diamond and the discrete duality schemes, one sets three discrete directional derivatives resolved in terms of a local basis, provided by the opposite faces for each hexahedron. This strategy allows the reconstruction of the gradient on the entire cell and therefore the mesh. Then, the numerical scheme stems from the discrete weak formulation. The proofs of the stability results, such as the discrete Poincaré's inequality or the derivation of the energy estimate, follows the guidelines of the literature. As a consequence, the stiffness matrix is symmetric positive-definite and the scheme stencil is small and compact in the sense that any node is connected to at most 26 neighbouring nodes in the case of Cartesian meshes. The resulting linear scheme is solved using the conjugate gradient method. This method exhibits some inefficiency when the mesh is severely distorted and the diffusion tensor is highly anisotropic. We therefore implemented the SSOR (symmetric successive over-relaxation) preconditioner [31] in order to improve the convergence behaviour of the linear solver.

The second contribution consists in the application of the 3D face interpolated scheme to the computation of the effective macroscopic thermal conductivity of wood. Thanks to image processing, the employed meshes are generated from the scanned real morphology of the sample. Then, the property is estimated following the orthotropic directions of wood. Compared to some recent works, the proposed numerical scheme is capable to recover similar ranges of the property in an excellent way and despite of the mesh deformation.

The rest of the paper is outlined as follows. In the next section, we survey the domain meshing and elaborate the approximation of the gradient operator. Then, we derive the 3D face interpolated discretisation method and study its stability together with solvability. In Section 3, we implement the numerical scheme and report the obtained results to confirm the efficiency and the robustness of our

methodology. In Section 4, we put into practice the 3D face interpolated scheme for the prediction of thermal conductivity of wood. The paper is then concluded in Section 5.

2 Numerical scheme

In this section we present the discretisation of the domain Ω. We introduce a consistent and accurate approximation of the gradient operator, and then derive the proposed 3D face interpolated scheme approximating the diffusion model (2).

2.1 Mesh, notations and discrete gradient

The mesh $\mathfrak{M}$ is given by a collection of conforming hexahedral cells $\{K\}$ that cover the whole domain Ω. We assume that the volume faces are planar. In other words, the scheme does not handle generalised hexahedra with non-planar faces. The centre of the cell is determined by averaging the coordinates of its surrounding vertices. The volume of K is denoted by $|K|$. Each cell possess six faces that are expressed as $\mathcal{F}_i, i \in \{1, \cdots, 6\}$. We denote by $x_{\mathcal{F}_i}$ the barycentre of the face $\mathcal{F}_i$. Let $\mathcal{T}$ denote the set of vertices of the mesh, and let $\mathcal{T}^D$ denote the set of boundary vertices. Let $\mathfrak{M}_{\mathbf{s}}$ represent the cells sharing the same vertex $\mathbf{s}$. For all $\mathbf{s} \in \mathcal{T}$, we assign a local sub-set $\omega_{K,\mathbf{s}}$ in the cell K, determined by the centre of the latter, the centres of the edges, and the faces sharing the same vertex, see Figure 1. The volume of $\omega_{K,\mathbf{s}}$ is computed using the identity

$$|\omega_{K,\mathbf{s}}| = |\mathrm{Det}\big(\overrightarrow{x_{\mathbf{s}}x}_{e^1_{K,\mathbf{s}}}, \overrightarrow{x_{\mathbf{s}}x}_{e^2_{K,\mathbf{s}}}, \overrightarrow{x_{\mathbf{s}}x}_{e^3_{K,\mathbf{s}}}\big)|,$$

where $e^1_{1,\mathbf{s}}$, $e^2_{2,\mathbf{s}}$, $e^3_{K,\mathbf{s}}$ are the edges of K whose extremity is $\mathbf{s}$. Therefore, the total sub-volume associated with $\mathbf{s}$ and its measure are defined by

$$\omega_{\mathbf{s}} = \bigcup_{K \in \mathfrak{M}_{\mathbf{s}}} \omega_{K,\mathbf{s}}, \quad |\omega_{\mathbf{s}}| = \sum_{K \in \mathfrak{M}_{\mathbf{s}}} |\omega_{K,\mathbf{s}}|.$$

The sum of these sub-volumes is equal to the volume of Ω. For $i \in \{1, 2, 3\}$, let us fix the vector $\overrightarrow{\boldsymbol{\tau}_{\mathcal{F}_{2i-1}\mathcal{F}_{2i}}} = \overrightarrow{x_{\mathcal{F}_{2i-1}}x_{\mathcal{F}_{2i}}}$. The set $\mathcal{T}_{\mathcal{F}_i}$ contains the four vertices of the face $\mathcal{F}_i$.

Let h_K denote the diameter of the cell $K \in \mathfrak{M}$. The mesh size is given by $h_{\mathcal{T}} = \max\{h_K, K \in \mathfrak{M}\}$. We denote by r_K the radius of the largest sphere included in K. Consider

$$\theta_{\mathcal{T}} = \max_{K \in \mathfrak{M}} \frac{h_K}{r_K}, \quad n_{\mathcal{T}} = \max_{\mathbf{s} \in \mathcal{T}} \#\mathfrak{M}_{\mathbf{s}}, \quad \xi_{\mathcal{T}} = \max(\theta_{\mathcal{T}}, n_{\mathcal{T}}).$$

As $\mathcal{T}$ is refined, the mesh regularity assumption states that $\xi_{\mathcal{T}}$ must be bounded with constant $\xi_0 > 0$ i.e., $\xi_{\mathcal{T}} \leq \xi_0$.

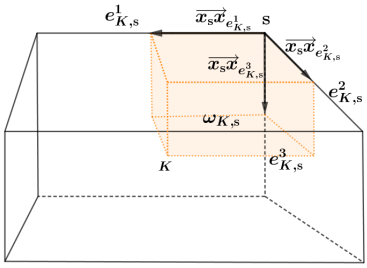

Figure 1: Sub-set associated with the vertex **s** in the cell K.

In hexahedral meshes it is not evident how to construct a nodal (i.e., primary unknowns are nodal) accurate approximation of only one gradient without auxiliary unknowns, or without using the traditional shape functions of the well-known finite element framework.

The key point of our approach lies in the definition of a consistent whole discrete gradient per cell. The six faces of K yield three noncollinear directions forming a local basis in 3D, see Figure 2. First, in each cell K, we begin to set the approximation of the gradient to the formula

$$\nabla_K u_{\mathcal{T}} = \frac{1}{|K|}\Big(\big(u_{\mathcal{F}_2} - u_{\mathcal{F}_1}\big)\overrightarrow{N_{12}} + \big(u_{\mathcal{F}_4} - u_{\mathcal{F}_3}\big)\overrightarrow{N_{34}} + \big(u_{\mathcal{F}_6} - u_{\mathcal{F}_5}\big)\overrightarrow{N_{56}} \Big), \qquad (3)$$

where

$$\overrightarrow{N_{12}} = \overrightarrow{\boldsymbol{\tau}_{\mathcal{F}_3\mathcal{F}_4}} \wedge \overrightarrow{\boldsymbol{\tau}_{\mathcal{F}_5\mathcal{F}_6}}, \quad \overrightarrow{N_{34}} = \overrightarrow{\boldsymbol{\tau}_{\mathcal{F}_5\mathcal{F}_6}} \wedge \overrightarrow{\boldsymbol{\tau}_{\mathcal{F}_1\mathcal{F}_2}}, \quad \overrightarrow{N_{56}} = \overrightarrow{\boldsymbol{\tau}_{\mathcal{F}_1\mathcal{F}_2}} \wedge \overrightarrow{\boldsymbol{\tau}_{\mathcal{F}_3\mathcal{F}_4}}.$$

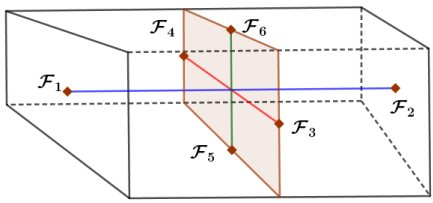

Figure 2: opposite faces in the cell K and their corresponding directions.

An important observation is that the total number of faces of the mesh is larger than the number of vertices of the mesh. Consequently, the degrees of freedom are placed on the mesh vertices in order to reduce the complexity of the numerical scheme. For this purpose, because the faces are planar, the face unknowns can be

eliminated by considering the second order interpolation

$$u_{\mathcal{F}_i} = \frac{1}{4} \sum_{\mathbf{s} \in \mathcal{T}_{\mathcal{F}_i}} u_{\mathbf{s}}.$$

To simplify the exposition, we assume that the boundary datum g can be extended to a function that is still denoted $g \in H^1(\Omega)$. This gives sense to the following integral approximation for the average of the function over the volume $\omega_{\mathbf{s}}$

$$g_{\mathbf{s}} = \frac{1}{|\omega_{\mathbf{s}}|} \int_{\omega_{\mathbf{s}}} g(a) \, \mathrm{d}a.$$

Define $\mathbb{R}^{\#\mathcal{T}}$ to be the finite dimensional space containing vectors of the form $u_{\mathcal{T}} = (u_{\mathbf{s}})^t_{\mathbf{s} \in \mathcal{T}}$. We denote by $\mathbb{R}^{\#\mathcal{T}}_g$ (resp. $\mathbb{R}^{\#\mathcal{T}}_0$) the subspace for which $u_{\mathcal{T}}$ is such that $u_{\mathbf{s}} = g_{\mathbf{s}}$ (resp. $u_{\mathbf{s}} = 0$), for all $\mathbf{s} \in \mathcal{T}^D$. For each $u_{\mathcal{T}} \in \mathbb{R}^{\#\mathcal{T}}$, we associate a unique function $\mathcal{I}_h u_{\mathcal{T}}$ of $L^2(\Omega)$ that is expressed as

$$\mathcal{I}_h u_{\mathcal{T}} = \sum_{\mathbf{s} \in \mathcal{T}} u_{\mathbf{s}} \mathbf{1}_{\omega_{\mathbf{s}}},$$

where $\mathbf{1}_{\omega_{\mathbf{s}}}$ is the indicator function of the subset $\omega_{\mathbf{s}}$, i.e. $\mathbf{1}_{\omega_{\mathbf{s}}}(x) = 1$ for $x \in \omega_{\mathbf{s}}$ and is equal to 0 otherwise. Let ∇_h be the piecewise operator mapping $u_{\mathcal{T}} \in \mathbb{R}^{\#\mathcal{T}}$ into $\nabla_h u_{\mathcal{T}} \in L^2(\Omega)^3$ where

$$\nabla_h u_{\mathcal{T}} = \sum_{K \in \mathfrak{M}} \mathbf{1}_K \nabla_K u.$$

The tensor Λ is approximated by $\Lambda^h_{\mathfrak{M}}$ where the latter is piecewise constant on the cells of the mesh and written

$$\Lambda^h_{\mathfrak{M}} = \sum_{K \in \mathfrak{M}} \mathbf{1}_K \Lambda_K, \quad \Lambda_K = \frac{1}{|K|} \int_K \Lambda(x) \, \mathrm{d}x.$$

Define the norm $\|\cdot\|_{0,2}$ and the semi-norm $\|\cdot\|_{1,2}$ on $\mathbb{R}^{\#\mathcal{T}}$ such that

$$\|v_{\mathcal{T}}\|_{0,2} = \left(\sum_{\mathbf{s} \in \mathcal{T}} |\omega_{\mathbf{s}}| v_{\mathbf{s}}^2 \right)^{1/2}, \quad \|v_{\mathcal{T}}\|_{1,2} = \left(\sum_{K \in \mathfrak{M}} |K| |\nabla_K v_{\mathcal{T}}|^2 \right)^{1/2}.$$

2.2 3D face interpolated scheme

Having the discrete gradient at hand, the 3D face interpolated scheme is naturally derived from the discrete variational formulation: i.e., find $u_{\mathcal{T}} \in \mathbb{R}^{\#\mathcal{T}}_g$ satisfying the relationship

$$\int_\Omega \Lambda^h_{\mathfrak{M}} \nabla_h u_{\mathcal{T}} \cdot \nabla_h \varphi_{\mathcal{T}} \, \mathrm{d}x = \int_\Omega f \mathcal{I}_h \varphi_{\mathcal{T}} \, \mathrm{d}x, \quad \forall \varphi_{\mathcal{T}} \in \mathbb{R}^{\#\mathcal{T}}_0. \tag{4}$$

The pointwise version of the scheme can be equivalently given by

$$\begin{cases} \sum_{K \in \mathfrak{M}_{\mathbf{s}}} |K| \Lambda_K \nabla_K u_{\mathcal{T}} \cdot \nabla_K e_{\mathbf{s}} = |\omega_{\mathbf{s}}| f_{\mathbf{s}}, \quad \forall \mathbf{s} \in \mathcal{T} \setminus \mathcal{T}^D, \\ u_{\mathbf{s}} = g_{\mathbf{s}} \quad \forall \mathbf{s} \in \mathcal{T}^D, \end{cases} \tag{5}$$

where $\{e_s\}_{\mathbf{s} \in \mathcal{T}}$ denotes the canonical basis of $\mathbb{R}^{\#\mathcal{T}}$. For the sake of simplicity, assume that $g = 0$. The scheme (5) can then be recast in the matrix form

$$A_{\mathcal{T}} u_{\mathcal{T}} = F_{\mathcal{T}}, \tag{6}$$

where

$$(F_{\mathcal{T}})_{\mathbf{s}} = \begin{cases} |\omega_{\mathbf{s}}| f_{\mathbf{s}}, & \text{if } \mathbf{s} \in \mathcal{T} \setminus \mathcal{T}^D, \\ 0 & \text{if } \mathbf{s} \in \mathcal{T}^D. \end{cases}$$

The matrix $A_{\mathcal{T}}$ contains the stiffness coefficients. In view of the implementation perspective, the formulation (5) is not adequate. In practice, a possible way to fill $A_{\mathcal{T}}$ is described in the sequel. For this purpose, let us consider the numbering strategy illustrated in Figure 3. Each vertex of the cell K belongs to three faces of the same cell. Using this orientation convention, the expression of the gradient

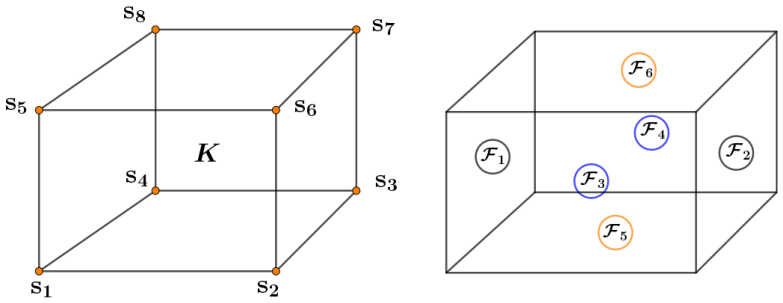

Figure 3: Numbering of the vertices (left) and the faces (right) of the cell K.

already described in (3) is now rewritten as follows

$$\nabla_K u_{\mathcal{T}} = \sum_{j=1}^{8} u_j a_j^K,$$

where the vectors $(a_j^K)_{1 \le j \le 8}$ are given by

$$a_1^K = \frac{1}{4|K|} \left(-\overrightarrow{N_{12}} - \overrightarrow{N_{34}} - \overrightarrow{N_{56}} \right), \quad a_2^K = \frac{1}{4|K|} \left(+\overrightarrow{N_{12}} - \overrightarrow{N_{34}} - \overrightarrow{N_{56}} \right),$$

$$a_3^K = \frac{1}{4|K|}\left(+\overrightarrow{N_{12}} + \overrightarrow{N_{34}} - \overrightarrow{N_{56}}\right), \quad a_4^K = \frac{1}{4|K|}\left(-\overrightarrow{N_{12}} + \overrightarrow{N_{34}} - \overrightarrow{N_{56}}\right),$$
$$a_5^K = \frac{1}{4|K|}\left(-\overrightarrow{N_{12}} - \overrightarrow{N_{34}} + \overrightarrow{N_{56}}\right), \quad a_6^K = \frac{1}{4|K|}\left(+\overrightarrow{N_{12}} - \overrightarrow{N_{34}} + \overrightarrow{N_{56}}\right),$$
$$a_7^K = \frac{1}{4|K|}\left(+\overrightarrow{N_{12}} + \overrightarrow{N_{34}} + \overrightarrow{N_{56}}\right), \quad a_8^K = \frac{1}{4|K|}\left(-\overrightarrow{N_{12}} + \overrightarrow{N_{34}} + \overrightarrow{N_{56}}\right).$$

As a consequence, the stiffness coefficients of the matrix $A_{\mathcal{T}}$ read

$$\begin{cases} (A_{\mathcal{T}})_{\mathbf{s}_i\mathbf{s}_i} = \displaystyle\sum_{K\in\mathfrak{M}_{\mathbf{s}_i}}\sum_{j=1}^{8}|K|\Lambda_K a_i^K\cdot a_j^K, & \text{if } \mathbf{s}_i \in \mathcal{T}\setminus\mathcal{T}^D, \\ (A_{\mathcal{T}})_{\mathbf{s}_i\mathbf{s}_j} = \displaystyle\sum_{K\in\mathfrak{M}_{\mathbf{s}_i}\cap\mathfrak{M}_{\mathbf{s}_j}}|K|\Lambda_K a_i^K\cdot a_j^K, & \text{if } \mathbf{s}_i \neq \mathbf{s}_j \in \mathcal{T}\setminus\mathcal{T}^D, \\ (A_{\mathcal{T}})_{\mathbf{s}_i\mathbf{s}_i} = 1, & \text{if } \mathbf{s}_i \in \mathcal{T}^D, \\ (A_{\mathcal{T}})_{\mathbf{s}_i\mathbf{s}_j} = 0, & \text{if } \mathbf{s}_i \in \mathcal{T}\setminus\mathcal{T}^D, \text{ and } \mathbf{s}_j \in \mathcal{T}^D, \\ (A_{\mathcal{T}})_{\mathbf{s}_i\mathbf{s}_j} = 0, & \text{if } \mathbf{s}_i \in \mathcal{T}^D, \text{ and } \mathbf{s}_i \neq \mathbf{s}_j, \end{cases}$$

where Λ_K is approximated by its value at the centre of the cell for the numerical computations. The above strategy has been used in the implementation of the scheme in Section 3.

Remark 1. *The stencil of the 3D face interpolated scheme is small and compact. In other words, each row of the matrix consists of at least one non-zero element and at most 27 non-zero elements in the case of Cartesian meshes. In the latter case, the diagonal element corresponds to an internal vertex, which is connected to its 26 surrounding vertices.*

As a result of the following discrete Poincaré's inequality, the semi-norm $\|\cdot\|_{1,2}$ turns out to be a norm on the subspace $\mathbb{R}_0^{\#\mathcal{T}}$.

Lemma 1 *There exists a constant C_p depending only on the diameter of Ω and the mesh regularity such that*

$$\|v_{\mathcal{T}}\|_{0,2} \leq C_p\|v_{\mathcal{T}}\|_{1,2}, \quad \forall v_{\mathcal{T}} \in \mathbb{R}_0^{\#\mathcal{T}}.$$

Proof The guidelines of the proof are sketched below. Let $\mathbf{s}_i \in K$. Observe that

$$\nabla_K v_{\mathcal{T}} = \sum_{j=1, j\neq i}^{8} a_j^K\left(v_{\mathbf{s}_j} - v_{\mathbf{s}_i}\right).$$

The regularity of the mesh claim the existence of C_1, C_2 depending only on $\theta_{\mathcal{T}}$ such that

$$\frac{C_0}{h_K^2} \leq |a_i^K\cdot a_j^K| \leq \frac{C_1}{h_K^2} \tag{7}$$

Then, it can be checked that

$$\|v_{\mathcal{T}}\|_{1,2}^2 \geq C_3 \sum_{\mathbf{s}_i \in \mathcal{T}} \sum_{K \in \mathfrak{M}_{\mathbf{s}_i}} \sum_{j=1, j\neq i}^{8} \frac{|K|}{h_K^2} \big(u_{\mathbf{s}_i} - u_{\mathbf{s}_j}\big)^2,$$

holds true for some C_3 independent of the mesh. Adapting of the proofs established in [5, Lemma 3.3], [14, Lemma 3.1] (in the case of the vertex-centred TPFA scheme) to our setting, one finds

$$\|v_{\mathcal{T}}\|_{0,2}^2 \leq C_4 \sum_{\mathbf{s}_i \in \mathcal{T}} \sum_{K \in \mathfrak{M}_{\mathbf{s}_i}} \sum_{j=1, j\neq i}^{8} h_K^2 |u_{\mathbf{s}_i} - u_{\mathbf{s}_j}| (|u_{\mathbf{s}_i}| + |u_{\mathbf{s}_j}|).$$

where C_4 depends only on $\theta_{\mathcal{T}}$ and the diameter of Ω. Following the arguments of [28, Lemma 2.1] and bearing in mind (7) we finally deduce that

$$\|v_{\mathcal{T}}\|_{0,2}^2 \leq C_5 \sum_{\mathbf{s}_i \in \mathcal{T}} \sum_{K \in \mathfrak{M}_{\mathbf{s}_i}} \sum_{j=1, j\neq i}^{8} \frac{|K|}{h_K^2} \big(u_{\mathbf{s}_i} - u_{\mathbf{s}_j}\big)^2 \leq C_p^2 \|v_{\mathcal{T}}\|_{1,2}^2,$$

which concludes the proof. □

In the rest of this section we prove that the numerical scheme is uniquely solvable. First, the following result is referred to as the coercivity property.

Proposition 2 *Let $u_{\mathcal{T}}$ be a solution to the scheme (5). The norm of the discrete gradient of $u_{\mathcal{T}}$ is bounded by a constant C_e depending only on, f, λ_0, λ_1, g and the mesh regularity i.e.,*

$$\|u_{\mathcal{T}}\|_{1,2} \leq C_e.$$

Proof Let us consider $g_{\mathcal{T}} \in \mathbb{R}_g^{\#\mathcal{T}}$ such that $(g_{\mathcal{T}})_{\mathbf{s}} = g_{\mathbf{s}}$ for all $\mathbf{s} \in \mathcal{T}$. Let us also take $\varphi_{\mathcal{T}} = \widehat{u}_{\mathcal{T}} := u_{\mathcal{T}} - g_{\mathcal{T}} \in \mathbb{R}_0^{\#\mathcal{T}}$ in (4). Then, one writes

$$Z_1 = Z_2 + Z_3,$$

where

$$Z_1 = \int_\Omega \Lambda_{\mathfrak{M}}^h \nabla_h \widehat{u}_{\mathcal{T}} \cdot \nabla_h \widehat{u}_{\mathcal{T}} \, \mathrm{d}x,$$
$$Z_2 = \int_\Omega \Lambda_{\mathfrak{M}}^h \nabla_h g_{\mathcal{T}} \cdot \nabla_h \widehat{u}_{\mathcal{T}} \, \mathrm{d}x,$$
$$Z_3 = \int_\Omega f \mathcal{I}_h \widehat{u}_{\mathcal{T}} \, \mathrm{d}x.$$

Because $\Lambda_{\mathfrak{M}}^h$ is coercive there holds $Z_1 \geq \lambda_0 \|\widehat{u}_{\mathcal{T}}\|_{1,2}^2$. It is known that, there exists C_1' depending only on ξ_0 such that

$$\|g_{\mathcal{T}}\|_{1,2} \leq C_1' \|g\|_{H^1(\Omega)}. \tag{8}$$

Then, using (8) together with the Cauchy-Schwarz and Young's inequalities we find

$$|Z_2| \leq \frac{\lambda_0}{4} \|\widehat{u}_{\mathcal{T}}\|_{1,2}^2 + \frac{\lambda_1 (C_1')^2}{\lambda_0} \|g\|_{H^1(\Omega)}^2.$$

Applying the Cauchy-Schwarz, Poincaré's and Young's inequalities allows us to obtain the estimation

$$|Z_3| \leq \frac{\lambda_0}{4}\|\widehat{u}_{\mathcal{T}}\|_{1,2}^2 + \frac{C_p^2\|f\|_{L^2(\Omega)}^2}{\lambda_0}.$$

Consequently, one obtains $\|\widehat{u}_{\mathcal{T}}\|_{1,2} \leq C_2'$, for some constant C_2' depending only on the data and ξ_0. We finally deduce

$$\|u_{\mathcal{T}}\|_{1,2} \leq \|g_{\mathcal{T}}\|_{1,2} + \|\widehat{u}_{\mathcal{T}}\|_{1,2} \leq C_e.$$

The proof is then concluded. □

Proposition 3 *The numerical scheme (5) has a unique solution.*

Proof It suffices to prove that the kernel of $A_{\mathcal{T}}$ is trivial. Let $X_{\mathcal{T}} \in \mathbb{R}^{\#\mathcal{T}}$ such that $A_{\mathcal{T}}X_{\mathcal{T}} = 0$. Let us prove that $X_{\mathcal{T}} = 0$. By the definition of $A_{\mathcal{T}}$, one has $(X_{\mathcal{T}})_{\mathbf{s}} = 0$ for all $\mathbf{s} \in \mathcal{T}^D$. Thus, $X_{\mathcal{T}} \in \mathbb{R}_0^{\#\mathcal{T}}$. Recall that the formulations (5)-(6) are equivalent. It follows from the computations

$$\begin{aligned} 0 &= A_{\mathcal{T}}X_{\mathcal{T}} \cdot X_{\mathcal{T}} \\ &= \sum_{\mathbf{s}\in\mathcal{T}\setminus\mathcal{T}^D} \sum_{K\in\mathfrak{M}_{\mathbf{s}}} |K|\Lambda_K \nabla_K u_{\mathcal{T}} \cdot X_{\mathbf{s}} \nabla_K e_{\mathbf{s}} \\ &= \int_\Omega \Lambda_{\mathfrak{M}}^h \nabla_h X_{\mathcal{T}} \cdot \nabla_h X_{\mathcal{T}} \,\mathrm{d}x \geq \lambda_0 \|X_{\mathcal{T}}\|_{1,2}, \end{aligned}$$

where we have again used the fact that $\Lambda_{\mathfrak{M}}^h$ is coercive. Hence, it must be that $\|X_{\mathcal{T}}\|_{1,2} = 0$, implying $X_{\mathcal{T}} = 0$, because $\|X_{\mathcal{T}}\|_{1,2}$ is a norm on $\mathbb{R}_0^{\#\mathcal{T}}$. This concludes the proof. □

Mimicking the previous proof entails that the matrix $A_{\mathcal{T}}$ is symmetric positive-definite.

3 Computational results

In this section, several test cases are simulated to assess the computational performance of the proposed numerical scheme. The first objective is to test the accuracy of the developed 3D face interpolated scheme and investigate its robustness with respect to the anisotropy and the distortion of the mesh. The second aim is to illustrate the behaviour of the iterative solver in the presence, and the absence of the preconditioner.

The computational domain Ω is the unit cube $[0,1]^3$. It is covered using four different partitions. They are referred to as the Cartesian, Kershaw, fluctuated and sinusoidal meshes respectively, see Figure 4. The first mesh is regular with cubic cells. The second mesh is taken from [16, 21]. The last two meshes are generated from the Cartesian mesh by transforming the old coordinates (x, y, z), that do not belong to the boundary edges, into the new positions (x', y', z') defined as follows

$$x' = x + \frac{1}{10}\varphi(x)\varphi(y), \quad y' = y + \frac{1}{10}\varphi(y)\varphi(z), \quad z' = z + \frac{1}{10}\varphi(x)\varphi(z),$$

where $\varphi(r) = \sin(2\pi r)$ in the case of the sinusoidal mesh and

$$\varphi(r) = 4r\mathbf{1}_{[0,0.5]} + (2-4r)\mathbf{1}_{[0.25,0.5]} + (4r-2)\mathbf{1}_{[0.5,0.75]} + (4-4r)\mathbf{1}_{[0.75,1]},$$

for the fluctuated mesh.

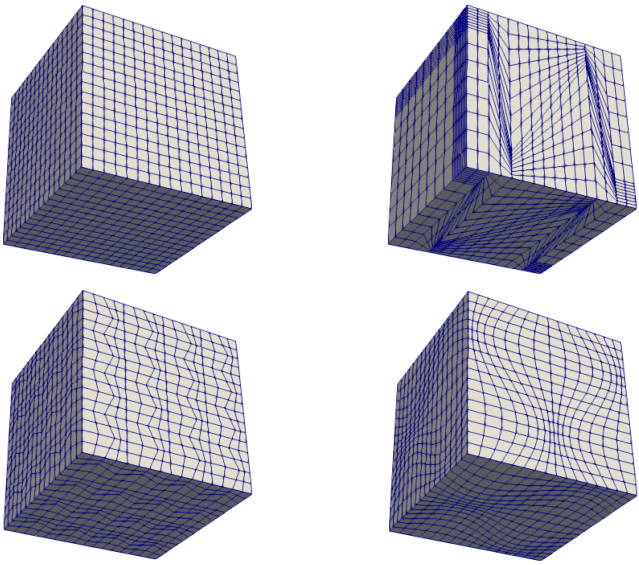

Figure 4: Cartesian, Kershaw, fluctuated and sinusoidal meshes.

Table 1 reports the number of degrees of freedom, dimension and sparsity of the stiffness matrix for each mesh level.

Mesh Nb	Nb of DOFs	Nb NzCoefffMat	Density
1	729	15625	2.94011 %
2	4913	117649	0.48741 %
3	35937	912673	0.07066 %
4	274625	7189057	0.00953 %
5	2097152	57066625	0.00129 %

Table 1: DOFs for each mesh and the corresponding number of non zero coefficients of the stiffness matrix.

The numerical scheme is implemented in Fortran where the resulting linear system is solved using the conjugate gradient method. Its tolerance is fixed to 10^{-10} and the stopping criterion is taken on the norm of the successive iterates. We employ the SSOR preconditioner to improve the solver behaviour. Recall that the stiffness matrix is denoted by $A_{\mathcal{T}}$. Let D be the diagonal component and E

the strictly lower triangular part of the stiffness matrix, so that $A_{\mathcal{T}} = D+E+E^T$. We consider the SSOR preconditioner, with relaxation parameter set as 1, given as follows

$$P = (D+E)D^{-1}(D+E^T). \tag{9}$$

We apply the preconditioner on the left of the stiffness matrix. Numerically, this choice without parametrization was found to give good results after the extensive numerical investigation performed in this study. Some indicators are needed in order to quantify the performance of the solver. We denote by κ the condition number of $A_{\mathcal{T}}$, and #it the total number of iterations of the conjugate gradient method. The biggest eigenvalue is denoted by λ. Let CPUt denote the computation time measured in seconds, before preconditioning. The same quantities are denoted by $\kappa^\star$, #it*, CPUt*, $\lambda^\star_{\max}$ after applying the preconditioner.

Five test cases are proposed below to test the performance of the numerical scheme in a progressive increase of the configuration severity:

- Case a : homogeneous and isotropic configuration,
- Case b : homogeneous configuration, but with an anisotropy ratio of 1000 along the z-axis,
- Case c : homogeneous and anisotropic configuration,
- Case d : anisotropic configuration, with material directions evolving in space,
- Case e : strongly discontinuous diffusion matrix (piece-wise variations).

In all cases, an analytical solution is imposed and the function f is set for this analytical solution to be a solution of problem (2). The accuracy of the scheme is assessed using the corresponding manufactured analytical. For this purpose, we evaluate the discrete L^2 and H^1 relative errors:

$$\frac{\|u_{e,\mathcal{T}} - u_{\mathcal{T}}\|_{0,2}}{\|u_{e,\mathcal{T}}\|_{0,2}}, \quad \sqrt{\frac{\|u_{e,\mathcal{T}} - u_{\mathcal{T}}\|^2_{0,2} + \|u_{e,\mathcal{T}} - u_{\mathcal{T}}\|^2_{1,2}}{\|u_{e,\mathcal{T}}\|^2_{0,2} + \|u_{e,\mathcal{T}}\|^2_{1,2}}},$$

where $u_{e,\mathcal{T}}$ is the interpolate (value) of the exact solution on the vertices.

3.1 Test case a

In this first test case involving a homogeneous medium, the diffusion tensor is taken as the identity matrix. The Dirichlet boundary conditions are computed according to the analytical solution

$$u_e(x,y,z) = \sin(2\pi x)\sin(2\pi x)\sin(2\pi z).$$

The right hand side f is

$$f(x,y,z) = 12\pi^2 \sin(2\pi x)\sin(2\pi x)\sin(2\pi z).$$

Figure 5 presents the log-log plots of the errors in terms of the mesh size. It is shown that the convergence rates of the method are second order for both norms.

Smaller convergence rates on the gradients are noticed on the first elements of the Kershaw meshes.

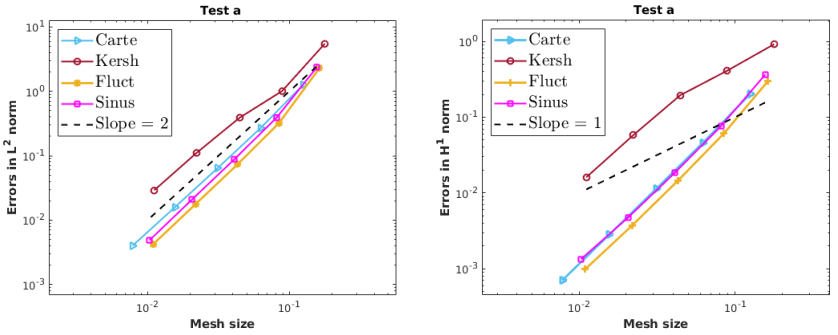

Figure 5: Test a : numerical relative errors in the L^2-norm (left) and H^1-norm (right).

The solver behaviour is given in Table 2. The condition number as well as the total number of iterations are greatly reduced after the preconditioning. This translates into gains in the CPU time. Interestingly, the iterations increased after preconditioning for the Cartesian mesh.

Cartesian meshes								
$h_{\mathcal{T}}$	κ	$\kappa^\star$	$\lambda_{\max}$	$\lambda^\star_{\max}$	#it	#it*	CPU	CPU*
0.125	8.30E+2	4.85E+1	1.00E+0	1.10E+0	18	12	0.0059	0.0044
0.063	2.61E+4	7.58E+2	1.00E+0	1.12E+0	21	11	0.0546	0.0417
0.031	8.31E+5	1.19E+4	1.00E+0	1.13E+0	40	20	0.4577	0.3482
Kershaw meshes								
$h_{\mathcal{T}}$	κ	$\kappa^\star$	$\lambda_{\max}$	$\lambda^\star_{\max}$	#it	#it*	CPU	CPU*
0.178	2.91E+3	8.98E+1	5.43E+0	1.12E+0	98	40	0.0129	0.0088
0.089	1.20E+5	5.13E+2	6.05E+0	1.06E+0	419	89	0.1864	0.0986
0.045	2.90E+6	1.39E+3	5.72E+0	1.15E+0	1158	134	3.1635	0.9512
Fluctuated meshes								
$h_{\mathcal{T}}$	κ	$\kappa^\star$	$\lambda_{\max}$	$\lambda^\star_{\max}$	#it	#it*	CPU	CPU*
0.163	8.76E+2	5.28E+1	1.00E+0	1.08E+0	49	24	0.0071	0.0100
0.085	2.60E+4	8.33E+2	1.00E+0	1.10E+0	107	37	0.0941	0.0611
0.043	8.31E+5	6.76E+3	1.00E+0	1.12E+0	77	27	0.5714	0.4546
Sinusoidal meshes								
$h_{\mathcal{T}}$	κ	$\kappa^\star$	$\lambda_{\max}$	$\lambda^\star_{\max}$	#it	#it*	CPU	CPU*
0.156	7.75E+2	4.80E+1	1.00E+0	1.06E+0	50	23	0.0096	0.0072
0.081	2.11E+4	7.93E+2	1.00E+0	1.12E+0	42	16	0.0760	0.0574
0.041	6.75E+5	7.86E+3	1.00E+0	1.13E+0	82	24	0.5812	0.4406

Table 2: Test a: solver statistics before and after the preconditioning.

3.2 Test case b

We now consider a global, highly anisotropic tensor in the z-direction

$$\Lambda = \begin{pmatrix} 1 & 0 & 0 \\ 0 & 1 & 0 \\ 0 & 0 & 1000 \end{pmatrix}.$$

The exact solution is given by

$$u_e(x, y, z) = 64x(1-x)y(1-y)z(1-z).$$

The source function corresponding to this solution is given by

$$f(x, y, z) = 128\Big(y(1-y)z(1-z) + x(1-x)z(1-z) + 1000x(1-x)y(1-y)\Big).$$

A homogeneous Dirichlet boundary condition is prescribed. The obtained results are displayed in Figure 6. The order of convergence is quadratic regardless of the anisotropy.

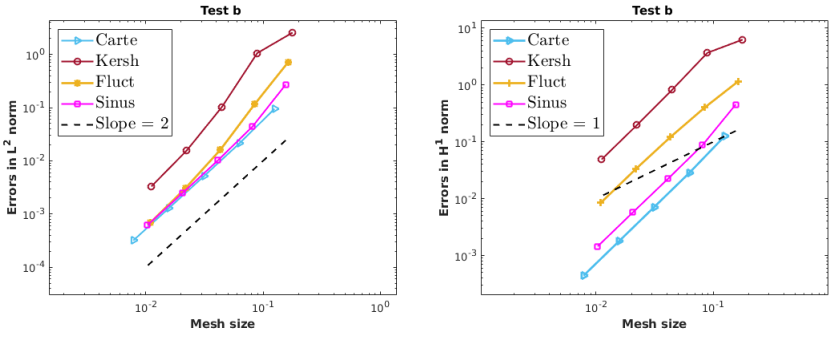

Figure 6: Test b : numerical relative errors in the L^2-norm (left) and H^1-norm (right).

Table 3 summarises the solver behaviour in the presence of a highly anisotropic tensor. Significant improvements in convergence rates of the iterative solver are observed after the application of the preconditioner, especially when the mesh is nonorthogonal and distorted.

Cartesian meshes								
$h_{\mathcal{T}}$	κ	$\kappa^\star$	$\lambda_{\max}$	$\lambda^\star_{\max}$	#it	#it*	CPU	CPU*
0.125	1.36E+4	4.77E+2	4.45E+2	1.01E+0	85	53	0.0364	0.0221
0.063	7.62E+4	2.90E+3	2.43E+2	1.02E+0	147	56	0.2403	0.1078
0.031	3.20E+5	8.62E+3	1.24E+2	1.05E+0	121	43	1.5471	0.8918
Kershaw meshes								
$h_{\mathcal{T}}$	κ	$\kappa^\star$	$\lambda_{\max}$	$\lambda^\star_{\max}$	#it	#it*	CPU	CPU*
0.178	1.45E+4	1.43E+2	7.89E+2	9.74E-1	285	84	0.0427	0.0335
0.089	2.38E+5	5.78E+2	9.17E+2	1.03E+0	1535	230	1.4538	0.1901
0.045	2.35E+6	3.57E+3	6.27E+2	1.12E+0	4599	484	12.1548	3.5647
Fluctuated meshes								
$h_{\mathcal{T}}$	κ	$\kappa^\star$	$\lambda_{\max}$	$\lambda^\star_{\max}$	#it	#it*	CPU	CPU*
0.163	6.95E+3	1.05E+2	5.65E+2	1.01E+0	244	57	0.0404	0.0227
0.085	8.78E+4	8.36E+2	4.03E+2	1.07E+0	765	135	0.4639	0.1537
0.043	1.40E+6	2.11E+3	2.57E+2	1.08E+0	1778	233	5.0515	1.0831
Sinusoidal meshes								
$h_{\mathcal{T}}$	κ	$\kappa^\star$	$\lambda_{\max}$	$\lambda^\star_{\max}$	#it	#it*	CPU	CPU*
0.156	4.74E+4	1.46E+2	7.36E+2	1.08E+0	332	69	0.0424	0.0248
0.081	1.13E+5	6.43E+2	5.30E+2	1.14E+0	830	122	0.4240	0.1005
0.041	1.32E+6	3.14E+3	3.17E+2	1.12E+0	703	101	2.9447	1.0333

Table 3: Test b: solver statistics before and after the preconditioning.

3.3 Test case c

In this example, we look at the behaviour of the discretisation scheme in the case where diffusion tensor is a fully heterogeneous and anisotropic matrix

$$\Lambda = \begin{pmatrix} y^2+z^2+1 & -xy & -xz \\ -xy & x^2+z^2+1 & -yz \\ -xz & -yz & x^2+y^2+1 \end{pmatrix}.$$

This tensor is inspired from [22]. The analytical solution is set to

$$u_e(x,y,z) = x^2yz^3 + x\cos(\pi y)\cos(\pi z),$$

where the right-hand side and nonhomogeneous Dirichlet boundary condition agree with this function. The numerical results are exhibited in Figure 7. The accuracy is again of second order for the solution and the gradient. This confirms the robustness of our scheme with respect to the mesh and anisotropy.

Table 4 summaries the solver behaviour. Here again, the preconditioned system is better in terms of performance in the case of a heterogeneous tensor.

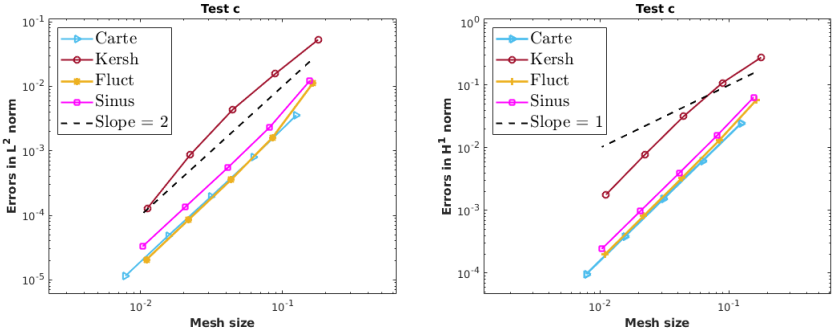

Figure 7: Test c : numerical relative errors in the L^2-norm (left) and H^1-norm (right).

Cartesian meshes								
$h_{\mathcal{T}}$	κ	$\kappa^\star$	$\lambda_{\max}$	$\lambda^\star_{\max}$	#it	#it*	CPU	CPU*
0.125	8.07E+2	4.57E+1	1.00E+0	1.11E+0	16	9	0.0274	0.0153
0.063	1.62E+4	7.22E+2	1.00E+0	1.14E+0	23	8	0.1933	0.1067
0.031	5.15E+5	7.66E+3	1.00E+0	1.16E+0	29	12	1.4337	0.9794
Kershaw meshes								
$h_{\mathcal{T}}$	κ	$\kappa^\star$	$\lambda_{\max}$	$\lambda^\star_{\max}$	#it	#it*	CPU	CPU*
0.178	3.08E+3	8.41E+1	8.81E+0	1.07E+0	104	39	0.0399	0.0191
0.089	1.22E+5	5.33E+2	1.00E+1	1.17E+0	441	81	0.3149	0.1235
0.045	3.71E+6	1.18E+3	1.03E+1	1.20E+0	352	47	2.3797	1.0002
Fluctuated meshes								
$h_{\mathcal{T}}$	κ	$\kappa^\star$	$\lambda_{\max}$	$\lambda^\star_{\max}$	#it	#it*	CPU	CPU*
0.163	1.17E+3	5.49E+1	1.26E+0	1.10E+0	48	19	0.0290	0.0111
0.085	2.44E+4	8.41E+2	1.00E+0	1.10E+0	44	16	0.2095	0.1008
0.043	4.99E+5	4.42E+3	1.00E+0	1.14E+0	38	13	1.6345	1.0540
Sinusoidal meshes								
$h_{\mathcal{T}}$	κ	$\kappa^\star$	$\lambda_{\max}$	$\lambda^\star_{\max}$	#it	#it*	CPU	CPU*
0.156	1.10E+3	5.14E+1	1.37E+0	1.10E+0	37	15	0.0400	0.0260
0.081	2.05E+4	8.28E+2	1.02E+0	1.14E+0	25	11	0.1977	0.0981
0.041	4.54E+5	6.22E+3	1.00E+0	1.17E+0	36	13	1.5419	1.0680

Table 4: Test c: solver statistics before and after the preconditioning.

3.4 Test case d

In this experiment, the eigenvectors directions change over the domain. Then, the diffusion tensor is decomposed as follows [17, 20]

$$\Lambda(x,y,z) = \mathcal{R}_\theta(x) \times \begin{pmatrix} 1 & 0 & 0 \\ 0 & \varepsilon & 0 \\ 0 & 0 & \eta(1+x+y+z) \end{pmatrix} \times \mathcal{R}_\theta(x)^t,$$

where $\varepsilon = 0.1$, $\eta = 10$ and

$$\mathcal{R}_\theta(x) = \begin{pmatrix} \cos(\pi x) & -\sin(\pi x) & 0 \\ \sin(\pi x) & \cos(\pi x) & 0 \\ 0 & 0 & 1 \end{pmatrix}.$$

We impose the exact solution to be

$$u_e(x, y, z) = \sin(\pi x)\sin(\pi x)\sin(\pi z).$$

The source term is routinely calculated from this solution. A homogeneous boundary condition is applied. The convergence results are plotted in Figure 8. Here we again observe the numerical optimal convergence rates in the L^2-norm and H^1-norm for the different meshes.

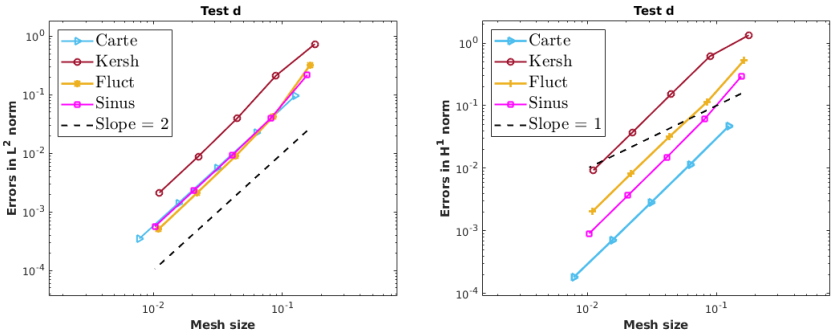

Figure 8: Test d : numerical relative errors in the L^2-norm (left) and H^1-norm (right).

The solver behaviour shown in Table 5 is consistent with the previous test case. We retain the impact of the preconditioner on reducing the CPU time, whereas the unpreconditioned solver requires considerably more iterations. This, for instance, is clearly apparent for the case of the Kershaw mesh.

3.5 Test case e

In this last example, we test our scheme in the case of a highly discontinuous diffusion matrix. We divide the domain Ω into two sub-domains Ω_1 and Ω_2 where

$$\Omega_1 = [0, 1] \times [0, 0.5] \times [0, 1], \quad \Omega_2 = [0, 1] \times [0.5, 1] \times [0, 1].$$

Following [3], the anisotropy tensor is respectively defined on Ω_1 and Ω_2 by

$$\Lambda_1 = \begin{pmatrix} \varrho+1 & \varrho & \varrho \\ \varrho & \varrho+1 & \varrho \\ \varrho & \varrho & \varrho+1 \end{pmatrix}, \qquad \Lambda_2 = \begin{pmatrix} \varrho+1 & -\varrho & \varrho \\ -\varrho & \varrho+1 & -\varrho \\ \varrho & -\varrho & \varrho+1 \end{pmatrix},$$

Cartesian meshes								
$h_{\mathcal{T}}$	κ	$\kappa^\star$	$\lambda_{\max}$	$\lambda^\star_{\max}$	#it	#it*	CPU	CPU*
0.125	2.47E+3	8.74E+1	1.22E+1	1.01E+0	66	27	0.0254	0.0153
0.063	2.69E+4	6.68E+2	7.43E+0	1.02E+0	46	18	0.1849	0.0905
0.031	4.53E+5	6.96E+3	4.17E+0	1.05E+0	74	14	1.4793	1.0899
Kershaw meshes								
$h_{\mathcal{T}}$	κ	$\kappa^\star$	$\lambda_{\max}$	$\lambda^\star_{\max}$	#it	#it*	CPU	CPU*
0.178	3.35E+3	5.72E+1	2.42E+1	1.10E+0	145	43	0.0321	0.0209
0.089	6.90E+4	2.22E+2	2.46E+1	1.05E+0	618	98	0.3600	0.1235
0.045	1.59E+6	1.08E+3	1.73E+1	1.12E+0	1017	111	3.8786	1.1868
Fluctuated meshes								
$h_{\mathcal{T}}$	κ	$\kappa^\star$	$\lambda_{\max}$	$\lambda^\star_{\max}$	#it	#it*	CPU	CPU*
0.163	3.49E+3	6.30E+1	1.66E+1	9.95E-1	131	37	0.0377	0.0211
0.085	7.39E+4	6.56E+2	1.32E+1	1.11E+0	342	64	0.2631	0.1088
0.043	1.41E+6	2.02E+3	8.68E+0	1.05E+0	284	44	2.1575	1.0610
Sinusoidal meshes								
$h_{\mathcal{T}}$	κ	$\kappa^\star$	$\lambda_{\max}$	$\lambda^\star_{\max}$	#it	#it*	CPU	CPU*
0.156	5.63E+3	6.63E+1	1.92E+1	1.08E+0	145	32	0.0294	0.0172
0.081	9.43E+4	5.74E+2	1.53E+1	1.05E+0	152	31	0.2138	0.1063
0.041	1.69E+6	1.96E+3	1.01E+1	1.13E+0	162	26	1.7939	0.9587

Table 5: Test d: solver statistics before and after the preconditioning.

where $\varrho \geq 0$. It can be checked that

$$u_e(x, y, z) = 2y^3 - 3y(\varrho + 1)(x - z)^2,$$

is the exact solution to the model with $f = 0$. The Dirichlet boundary condition is nothing more than the trace of u_e on $\partial\Omega$. The ratio of anisotropy is given by $3\varrho + 1$. In Figure 9, we exhibit the errors induced by the numerical scheme in the L^2-norm for $\varrho \in \{33, 3333\}$ leading to the ratio of anisotropy which is equal to 100 and 10000 respectively. One can observe that the convergence rate is of second order in both cases, independently of the last three meshes, and the scheme is exact on the Cartesian mesh.

In Table 6, a good performance of the new solver is observed. The reduction in the number of iterations as well as the CPU time is spectacular on the Kershaw mesh, which is a challenging mesh and accounts for a severe distortion. A similar behaviour is observed in the case where $\varrho = 333$.

4 Application to the prediction of wood thermal conductivity from its real 3D morphology

The objective here is to predict the effective thermal conductivity of wood using upscaling. One type of wood, namely poplar species is studied. For this purpose, we make use of high resolution scans provided by the Laboratory nano-tomograph and the proposed 3D face interpolated scheme to estimate the macroscopic property following the orthotropic directions of wood. For more details on the description

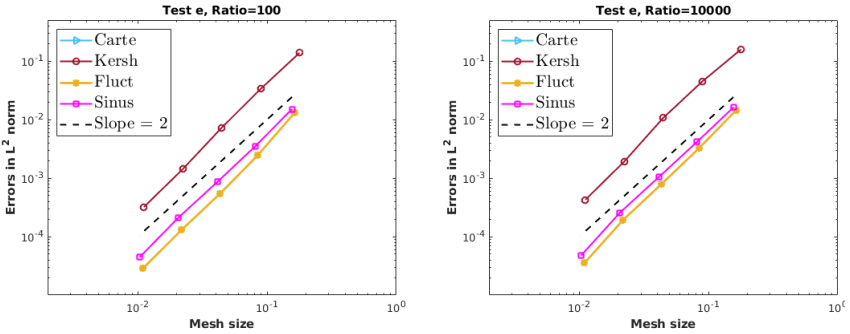

Figure 9: Test e: numerical relative errors in the L^2-norm (left) and H^1-norm (right).

Cartesian meshes								
$h_{\mathcal{T}}$	κ	$\kappa^\star$	$\lambda_{\max}$	$\lambda^\star_{\max}$	#it	#it*	CPU	CPU*
0.125	8.27E+2	5.40E+1	2.01E+1	1.13E+0	1	1	0.0239	0.0247
0.063	1.32E+4	8.73E+2	1.08E+1	1.18E+0	1	1	0.1645	0.1819
0.031	2.11E+5	1.29E+4	5.52E+0	1.17E+0	1	1	1.4829	1.5130
Kershaw meshes								
$h_{\mathcal{T}}$	κ	$\kappa^\star$	$\lambda_{\max}$	$\lambda^\star_{\max}$	#it	#it*	CPU	CPU*
0.178	7.17E+3	1.08E+2	2.50E+2	1.02E+0	235	70	0.0413	0.0248
0.089	3.22E+5	1.17E+3	2.76E+2	1.21E+0	1282	199	0.5264	0.1744
0.045	7.92E+6	2.50E+3	2.61E+2	1.29E+0	5147	480	12.8448	3.0689
Fluctuated meshes								
$h_{\mathcal{T}}$	κ	$\kappa^\star$	$\lambda_{\max}$	$\lambda^\star_{\max}$	#it	#it*	CPU	CPU*
0.163	1.61E+3	7.14E+1	3.07E+1	1.11E+0	90	29	0.0276	0.0160
0.085	3.41E+4	1.11E+3	2.22E+1	1.16E+0	241	71	0.2523	0.1081
0.043	6.54E+5	3.25E+3	1.48E+1	1.24E+0	392	80	2.1597	1.1155
Sinusoidal meshes								
$h_{\mathcal{T}}$	κ	$\kappa^\star$	$\lambda_{\max}$	$\lambda^\star_{\max}$	#it	#it*	CPU	CPU*
0.156	1.58E+3	7.40E+1	3.81E+1	1.13E+0	104	31	0.0285	0.0180
0.081	2.97E+4	1.18E+3	2.73E+1	1.16E+0	318	68	0.2754	0.1141
0.041	5.01E+5	4.55E+3	1.65E+1	1.21E+0	457	84	2.4813	1.0368

Table 6: Test e: solver statistics before and after the preconditioning for $\varrho = 33$.

of the sample preparation and the image processing of the scanned morphology, we refer to [23, 30].

An illustration of the scanned sample is exhibited in Figure 10. It is referred to as *Morpho*. Let us stress that it is quite difficult to make predictions on this whole volume. A standard practical alternative is to extract sub-volumes from the original morphology. Such a subset is called the REV (Representative Elementary Volume). The representativeness of the volume with respect the thermal conductivity is underlined below according to the convergence test.

We denote by $\Omega = \text{REV} = (x_0, x_m)\times(y_0, y_m)\times(z_0, z_p) \subset \textit{Morpho}$ the extracted region of interest. Its centre and dimensions are specified by the user. Then, one

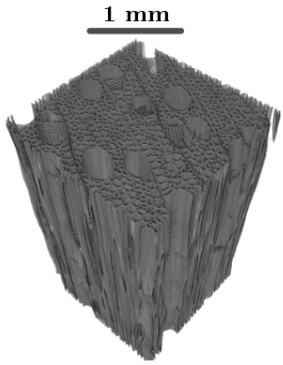

Figure 10: Scanned poplar sample using tomography with a resolution of $3\mu m$.

performs the automatic segmentation so that one obtains the binary 3D image and generate the orthogonal Cartesian mesh made from cubes. The thresholded morphology contains only two phases consisting of the air and the solid matrix as the left side of Figure 11. Its right side shows the sinusoidal perturbation of the real morphology. This modification intends to test the efficiency and the robustness of the 3D face interpolated scheme in predicting the thermal conductivity on a distorted sample.

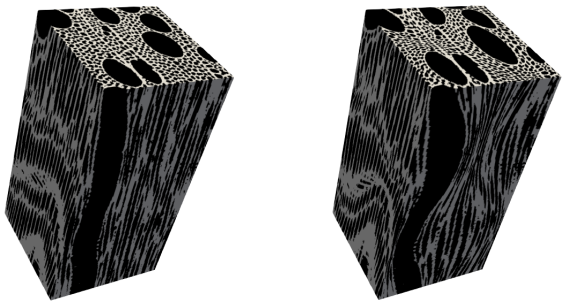

Figure 11: Original binary Cartesian morphology (left) and the corresponding sinusoidal perturbation (right)

The next step is to discretise Fourier's law on the morphology mesh thanks to the proposed 3D face interpolated scheme. The model problem writes

$$\begin{aligned} -\operatorname{div}\big(\alpha(x)\nabla T\big) &= 0, && \text{in} \quad \Omega = (x_0, x_m)\times(y_0, y_n)\times(z_0, z_p),\\ T &= T^{bd}, && \text{on} \quad \partial\Omega^D,\\ \alpha(x)\nabla T\cdot\vec{\mathbf{n}} &= 0, && \text{on} \quad \partial\Omega^N, \end{aligned}$$

where $\partial\Omega = \partial\Omega^D \cup \partial\Omega^N$ is the boundary and $\alpha = \lambda_0/(\varrho c_p)$ is the local thermal coefficient of each voxel (mesh vertex). It is composed of λ_0 the local thermal conductivity, ϱ the density and c_p the heat capacity. For computation, we take $\varrho c_p = 1$. The λ_0 is fixed to 0.5 W.m^{-1}.K^{-1} for the solid phase and 0.023 W.m^{-1}.K^{-1} for the air phase.

As we are going to run several computations, we select an increasing sequence of REVs, namely $\text{REV}_i = (x_0^i, x_m^i) \times (y_0^i, y_m^i) \times (z_0^i, z_p^i)$ where

$$x_0^i = y_0^i = z_0^i = 0, \quad x_m^i = y_n^i = \Big((32 \times i) - 1\Big) \times \text{Resolution},$$
$$z_p^i = \Big(((64 \times i) - 1) - 1\Big) \times \text{Resolution}, \quad \text{for } i = 1, \cdots, 5.$$

The resolution is given by $3.10^{-6}m$. For instance, the mesh of the first REV is made from $32 \times 32 \times 63$ vertices and so on.

The resulting linear system is solved by the preconditioned conjugate gradient method. The behaviour of the temperature gradient is highlighted in Figure 12. On the both meshes, it is clearly seen that the heat follows naturally the cell walls.

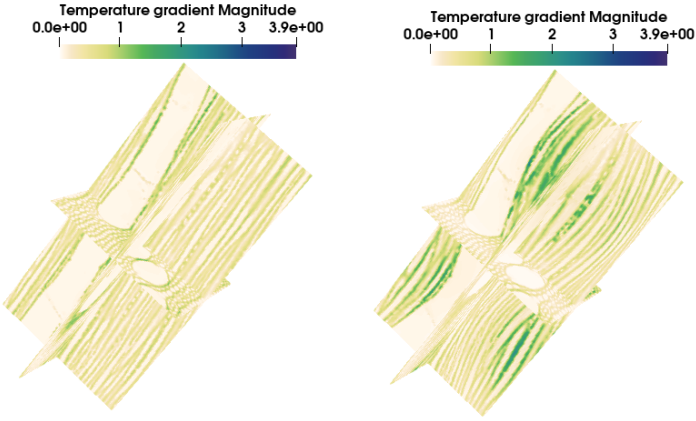

Figure 12: Gradient distribution of temperature on the Cartesian morphology (left) and on the sinusoidal one (right).

Accordingly, one can deduce the predicted thermal conductivity by assessing the ratio of the boundary flux $\langle \text{Flux}^{\text{bd}} \rangle$ to the global imposed gradient $\delta T/\text{Long}$ imposed by the taken boundary conditions. As a consequence, the radial, tangential and longitudinal directions conductivities are derived from

$$\lambda_R^t = \frac{\langle \text{Flux}_x^{\text{bd}} \rangle \times |x_m - x_0|}{\delta T}, \quad \lambda_\tau^t = \frac{\langle \text{Flux}_y^{\text{bd}} \rangle \times |y_n - y_0|}{\delta T},$$

$$\lambda_L^t = \frac{\langle \text{Flux}_z^{\text{bd}} \rangle \times |z_p - x_0|}{\delta T}.$$

The results are provided in Table 7. It reports the predicted macroscopic property in terms of the REV size. This convergence test shows that the property oscillates on the first volumes whereas it becomes to be stabilized as the REV size increases. Moreover, one can say that the REV5 is representative. On both meshes, the longitudinal value is bigger than the radial and tangential ones, which is in coherence with the wood structure. We also observe a slight reduction on the conductivity on the transformed morphology, which goes back to the impact of the waves induced by the sinusoidal perturbation. The results are similar to the ones obtained in [29, 30]. However, in these references the method is the standard TPFA finite volume which works only on orthogonal meshes and does not support anisotropy. This ensures the robustness of the proposed 3D face interpolated method in capturing the ranges of the thermal conductivity even on a distorted mesh.

Mesh	λ^t(W/(m.K))	REV1	REV2	REV3	REV4	REV5
Cartesian	λ_R^t	0.1906	0.1705	0.1430	0.1506	0.1522
	λ_τ^t	0.1841	0.1466	0.1336	0.1254	0.1314
	λ_L^t	0.2507	0.2238	0.2009	0.2021	0.2046
Sinusoidal	λ_R^t	0.1814	0.1657	0.1317	0.1418	0.1441
	λ_τ^t	0.1850	0.1511	0.1351	0.1266	0.1338
	λ_L^t	0.2386	0.2153	0.1864	0.1876	0.1920

Table 7: Predicted thermal conductivity of poplar with the real and the transformed morphology following the peculiar orthotropic directions of wood.

Table 8 indicates the solver performance. The first column lists the REV number. The second one informs the CPU time of the solver required to compute the three conductivities λ_R^t, λ_τ^t and λ_L^t. The last one provides the maximum of the errors committed in evaluating the latter values i.e.,

$$\text{Max residual} = \max\left(\text{Error}_{\lambda_R^t}, \text{Error}_{\lambda_\tau^t}, \text{Error}_{\lambda_L^t}\right).$$

One infers that the method is efficient and accurate on the Cartesian morphology, because the phases are quite well placed in parallel and ranged following the longitudinal direction compared to sinusoidal sample.

REV	CPU time (mins)		Max residual	
Number	Catre	Sinus	Catre	Sinus
REV1	5.11E-2	6.45E-2	2.18E-6	2.49E-3
REV2	4.55E-1	6.70E-1	3.79E-5	1.48E-3
REV3	2.23E+0	2.82E+0	5.48E-4	1.70E-3
REV4	7.05E+0	8.82E+0	6.04E-4	6.71E-4
REV5	1.81E+1	2.01E+1	3.59E-4	2.29E-2

Table 8: Solver performance.

5 Conclusion

In this paper, a new numerical method, referred to as the 3D face interpolated scheme, is proposed for the discretisation of highly anisotropic diffusion equations on hexahedral meshes. The idea consists in defining an accurate and consistent approximation of the gradient using the opposite faces of the cells. The face unknowns are eliminated by employing a second order interpolation. This reduces greatly the complexity of the scheme by placing the unknowns at the mesh nodes. Because the scheme is derived from a discrete weak formulation, it is unconditionally coercive and therefore admits a unique solution. As a result, the stiffness matrix is symmetric positive-definite. The numerical implementation makes use of the practical SSOR preconditioner in order to improve the behaviour of the iterative solver. The computational results show that the method is robust and attains second order accuracy independently of the chosen meshes and the anisotropy. After the validation step, the approach is applied for predicting the wood thermal conductivity in the species natural directions. Good results are obtained especially when the real morphology is perturbed using a sinusoidal transformation. In our future research we intend to extend this new methodology in a homogenisation framework for predicting the effective parameters of fibres with more than two phases that arise in volume-averaged transport equations.

Acknowledgments: This study was carried out in the Centre Européen de Biotechnologie et de Bioéconomie (CEBB), supported by the Région Grand Est, Département de la Marne, Greater Reims and the European Union. In particular, the author would like to thank the Département de la Marne, Greater Reims, Région Grand Est and the European Union along with the European Regional Development Fund (ERDF Champagne Ardenne 2014-2020) for their financial support of the Chair of Biotechnology of CentraleSupélec.

References

[1] Aavatsmark, I. 2002. An introduction to multipoint flux approximations for quadrilateral grids. *Computational Geosciences 6*(3): 405–432 .

[2] Aavatsmark, I., T. Barkve, O. Bøe, and T. Mannseth. 1998. Discretization on unstructured grids for inhomogeneous, anisotropic media. Part II: Discussion and numerical results. *SIAM Journal on Scientific Computing 19*(5): 1717–1736 .

[3] Aavatsmark, I., G.T. Eigestad, B.O. Heimsund, B.T. Mallison, J.M. Nordbotten, E. Øian, et al. 2010. A new finite-volume approach to efficient discretization on challenging grids. *SPE Journal 15*(03): 658–669 .

[4] Andreianov, B., M. Bendahmane, F. Hubert, and S. Krell. 2012. On 3D DDFV discretization of gradient and divergence operators. I. Meshing, operators and discrete duality. *IMA Journal of Numerical Analysis 32*(4): 1574–1603 .

[5] Andreianov, B., F. Boyer, and F. Hubert. 2007. Discrete duality finite volume schemes for Leray–Lions–type elliptic problems on general 2D meshes. *Numerical Methods for Partial Differential Equations 23*(1): 145–195 .

[6] Carr, E.J., I.W. Turner, and P. Perre. 2013. A dual-scale modeling approach for drying hygroscopic porous media. *Multiscale Modeling & Simulation 11*(1): 362–384 .

[7] Ciarlet, P.G. 2002. *The finite element method for elliptic problems*. SIAM.

[8] Coudière, Y., C. Pierre, O. Rousseau, and R. Turpault. 2009. A 2D/3D discrete duality finite volume scheme. Application to ECG simulation. *International Journal on Finite Volumes 6*(1): 24 .

[9] Coudière, Y., J.P. Vila, and P. Villedieu. 1999. Convergence rate of a finite volume scheme for a two dimensional convection-diffusion problem. *ESAIM: Mathematical Modelling and Numerical Analysis 33*(3): 493–516 .

[10] da Veiga, L.B., K. Lipnikov, and G. Manzini. 2014. *The mimetic finite difference method for elliptic problems*, Volume 11. Springer.

[11] Domelevo, K. and P. Omnes. 2005. A finite volume method for the Laplace equation on almost arbitrary two-dimensional grids. *M2AN. Mathematical Modelling and Numerical Analysis 39*(6): 1203–1249 .

[12] Droniou, J., R. Eymard, T. Gallouët, C. Guichard, and R. Herbin. 2018. *The gradient discretisation method*, Volume 82. Springer.

[13] Droniou, J., R. Eymard, T. Gallouët, and R. Herbin. 2010. A unified approach to mimetic finite difference, hybrid finite volume and mixed finite volume methods. *Mathematical Models and Methods in Applied Sciences 20*(02): 265–295 .

[14] Eymard, R., T. Gallouët, and R. Herbin. 2000. Finite volume methods, In *Handbook of numerical analysis*, eds. Ciarlet, P. and J. Lions, Volume 7, 713–1018. Elsevier. https://hal.archives-ouvertes.fr/hal-02100732v2.

[15] Eymard, R., T. Gallouët, and R. Herbin. 2010. Discretization of heterogeneous and anisotropic diffusion problems on general nonconforming meshes SUSHI: a scheme using stabilization and hybrid interfaces. *IMA Journal of Numerical Analysis 30*(4): 1009–1043 .

[16] Eymard, R., G. Henry, R. Herbin, F. Hubert, R. Klöfkorn, and G. Manzini. 2011. 3D benchmark on discretization schemes for anisotropic diffusion problems on general grids, In *Finite Volumes for Complex Applications VI Problems & Perspectives*, eds.

Fořt, J., J. Fürst, and F. Hubert, Volume 4, 895–930. Berlin, Heidelberg: Springer.

[17] Guillaume, P. and V. Latocha. 2005. Numerical convergence of a parameterisation method for the solution of a highly anisotropic two-dimensional elliptic problem. *Journal of Scientific Computing 25*(3): 423–444 .

[18] Herbin, R. and F. Hubert 2008. Benchmark on discretization schemes for anisotropic diffusion problems on general grids. In R. Eymard and J.-M. Herard (Eds.), *Finite Volumes for Complex Applications V*, pp. 659–692. Wiley.

[19] Hermeline, F. 2009a. A finite volume method for approximating 3D diffusion operators on general meshes. *Journal of Computational Physics 228*(16): 5763–5786 .

[20] Hermeline, F. 2009b. A finite volume method for approximating 3d diffusion operators on general meshes. *Journal of computational Physics 228*(16): 5763–5786 .

[21] Kershaw, D.S. 1981. Differencing of the diffusion equation in lagrangian hydrodynamic codes. *Journal of Computational Physics 39*(2): 375–395 .

[22] Lipnikov, K., M. Shashkov, and D. Svyatskiy. 2006. The mimetic finite difference discretization of diffusion problem on unstructured polyhedral meshes. *Journal of Computational Physics 211*(2): 473–491 .

[23] Louërat, M., M. Ayouz, and P. Perré. 2018. Heat and moisture diffusion in spruce and wood panels computed from 3-d morphologies using the lattice boltzmann method. *International Journal of Thermal Sciences* 130: 471–483 .

[24] Lux, J., A. Ahmadi, C. Gobbé, and C. Delisée. 2006. Macroscopic properties of real fibrous materials: Volume averaging method and 3d image analysis. *International Journal of Heat and Mass Transfer 49*(11-12): 1958–1973 .

[25] Perré, P., D.M. Nguyen, and G. Almeida. 2022. A macroscopic washburn approach of liquid imbibition in wood derived from x-ray tomography observations. *Scientific reports 12*(1): 1–14 .

[26] Perré, P. and I. Turner. 2001. Determination of the material property variations across the growth ring of softwood for use in a heterogeneous drying model. part 2. use of homogenisation to predict bound liquid diffusivity and thermal conductivity. *Holzforschung 55*(4): 417–425 .

[27] Perré, P. and I.W. Turner. 1999. A 3D version of Transpore: a comprehensive heat and mass transfer computational model for simulating the drying of porous media. *International Journal for Heat and Mass Transfer 42*(12): 4501–4521 .

[28] Quenjel, E.H. and A. Beljadid. 2022. Node-Diamond approximation of heterogeneous and anisotropic diffusion systems on arbitrary two-dimensional grids. *Mathematics and Computers in Simulation* 204: 450–472 .

[29] Quenjel, E.H. and P. Perré. October 2022. Efficient prediction of the thermal conductivity of wood from its microscopic morphology. *Accepted in Lecture Notes in Mechanical Engineering* .

[30] Quenjel, E.H. and P. Perrée. 2022. Computation of the effective thermal conductivity from 3d real morphologies of wood. *Heat and Mass Transfer 58*(12): 2195–2206 .

[31] Saad, Y. 2003. *Iterative methods for sparse linear systems*. SIAM.